ARL-TR-8308 ● MAR 2018

US Army Research Laboratory

Thermal Property Engineering: Exploiting the Properties of Ceramic Nanocomposites

by Zackery Fleischman, Victoria Blair, Nicholas Ku, Larry Merkle, Carli Moorehead, Aubrey Fry, Steven Kilczewski, Donovan Harris, and Robert Pavlacka

NOTICES

Disclaimers

The findings in this report are not to be construed as an official Department of the Army position unless so designated by other authorized documents.

Citation of manufacturer's or trade names does not constitute an official endorsement or approval of the use thereof.

Destroy this report when it is no longer needed. Do not return it to the originator.

ARL-TR-8308 ● MAR 2018

US Army Research Laboratory

Thermal Property Engineering: Exploiting the Properties of Ceramic Nanocomposites

by Zackery Fleischman
Sensors and Electron Devices Directorate, ARL

Victoria Blair
Weapons and Materials Research Directorate, ARL

Co-Contributors: Nicholas Ku, Larry Merkle, Carli Moorehead, Aubrey Fry, Steven Kilczewski, Donovan Harris, and Robert Pavlacka

REPORT DOCUMENTATION PAGE

Form Approved
OMB No. 0704-0188

1. REPORT DATE *(DD-MM-YYYY)*	2. REPORT TYPE	3. DATES COVERED (From - To)
March 2018	Director's Research Initiative (DRI) Report	Jan 1 2015 – Dec 31 2017

4. TITLE AND SUBTITLE

Thermal Property Engineering: Exploiting the Properties of Ceramic Nanocomposites

5a. CONTRACT NUMBER

5b. GRANT NUMBER

5c. PROGRAM ELEMENT NUMBER

6. AUTHOR(S)

Zackery Fleischman, Victoria Blair, Nicholas Ku, Larry Merkle, Carli Moorehead, Aubrey Fry, Steven Kilczewski, Donovan Harris, and Robert Pavlacka

5d. PROJECT NUMBER

5e. TASK NUMBER

5f. WORK UNIT NUMBER

7. PERFORMING ORGANIZATION NAME(S) AND ADDRESS(ES)

US Army Research Laboratory
ATTN: RDRL-SEE-L
Aberdeen Proving Ground, MD 21005-5066

8. PERFORMING ORGANIZATION REPORT NUMBER

ARL-TR-8308

9. SPONSORING/MONITORING AGENCY NAME(S) AND ADDRESS(ES)

10. SPONSOR/MONITOR'S ACRONYM(S)

11. SPONSOR/MONITOR'S REPORT NUMBER(S)

12. DISTRIBUTION/AVAILABILITY STATEMENT

Approved for public release; distribution is unlimited.

13. SUPPLEMENTARY NOTES

14. ABSTRACT

We developed dual-phase ceramic nanocomposites, as opposed to single-phase ceramics, as a potential laser gain material that could incorporate the low-maximum phonon energy necessary for efficient mid-infrared laser output with the high thermal conductivity needed for effective thermal management at high operating powers. Our materials were comprised of an undoped majority species (magnesium oxide) and a rare-earth doped minority species (erbium doped yttrium oxide). Nanocomposite powders were prepared using a novel co-precipitation method that allows for intimate mixing of the constituent species. The results of physical and optical characterization of the powders guided the synthesis parameters of subsequent batches toward optimal material conditions as defined by desired laser performance. Resultant powders went through various methods of densification followed by characterization to steer the parameters toward translucency.

15. SUBJECT TERMS

DRI, ceramic, nanocomposite, laser, rare earth scattering

16. SECURITY CLASSIFICATION OF:			17. LIMITATION OF ABSTRACT	18. NUMBER OF PAGES	19a. NAME OF RESPONSIBLE PERSON
a. REPORT	b. ABSTRACT	c. THIS PAGE			Zackery Fleischman
Unclassified	Unclassified	Unclassified	UU	40	19b. TELEPHONE NUMBER (Include area code) 301-394-1142

Standard Form 298 (Rev. 8/98)
Prescribed by ANSI Std. Z39.18

Contents

List of Figures

List of Tables

Acknowledgments

This research was supported in part by an appointment to the Postgraduate Research Participation Program at the US Army Research Laboratory (ARL) administered by the Oak Ridge Institute for Science and Education through an interagency agreement between the US Department of Energy and ARL.

The Principal Investigators would like to thank the ARL Fellows and Directors for their support on this program for the past 3 years. We did not expect to get 3 full years of funding and were grateful for the opportunity to see this work to its completion in the Director's Research Initiative program.

INTENTIONALLY LEFT BLANK.

1. Objective

The objective of this program is to develop a dual-phase ceramic-matrix nanocomposite, as opposed to a single-phase ceramic, as a laser gain medium that could incorporate the low maximum phonon energy necessary for efficient mid-infrared laser output with the high thermal conductivity needed for effective thermal management at high operating powers. The undoped majority species (magnesium oxide [MgO]) was chosen because of its relatively high thermal conductivity, and the rare earth (RE) doped minority species—erbium:yttrium oxide ($Er:Y_2O_3$) was chosen because of its low maximum phonon energy.

2. Overview

There has been much interest in lasers emitting in the mid-infrared spectral region for use in a wide array of application including atmospheric sensing,[1] infrared counter measure technologies, and optical pumping of longer wavelength solid-state lasers. However, a set of thermal management challenges arises in pursuit of high-output power lasers operating at mid-infrared wavelengths ($2\ \mu m < \lambda < 8\ \mu m$). The first challenge arises because of the close spacing between upper and lower laser levels in this spectral region, which makes luminescence quenching by multiphonon relaxation especially problematic. This quenching can be ameliorated by using gain materials with small maximum phonon energies. The second challenge originates from the fact that even the most efficient gain media convert some fraction of the pump energy into thermal energy. Buildup of this "waste heat" can result in serious beam problems such as thermal lensing and depolarization.[2,3] Unfortunately, a single material solution for these 2 challenges is hampered because the material requirements for low maximum phonon energy and high thermal conductivity are very often incompatible. This is due to light constituent ions most often needed for high thermal conductivity resulting in strong ion-ion interactions, and, hence, yielding large maximum phonon energies.

The solution to these challenges might be found in the use of polycrystalline, or ceramic, materials. The synthesis procedures of ceramic laser gain materials have matured in recent years such that their optical quality can be comparable to that of single crystals. In fact, RE doped yttrium aluminum garnet (YAG) ceramics have demonstrated similar or better laser efficiency compared to their single-crystal counterparts.[4,5] Polycrystalline ceramic materials offer a myriad of other benefits, as well including greater flexibility in size and shape, processing temperatures considerably lower than the crystal melting temperatures, and potentially lower costs.[6]

One aspect of ceramics that is particularly attractive when considering the challenges previously described is the ability to fashion multiphase materials composed of several different material species. Dual-phase ceramics, in particular, offer the potential to alleviate the problem of incompatible laser host requirements for low quenching and high thermal conductivity by incorporating multiple phases into the same structure to share the overall benefits of the individual constituent species. Recently, dual-phase ceramics composed of MgO and Y_2O_3 have been prepared to produce infrared-transmitting windows with increased durability and thermal shock resistance.[7–13] As shown in Fig. 1, to reduce optical scattering to laser and optical standards, the grain size must be substantially smaller than the wavelength of light,[14] meaning that the resultant ceramics will actually be a nanocomposite. This is especially important when there is a significant difference in the index of refraction between the different constituents.

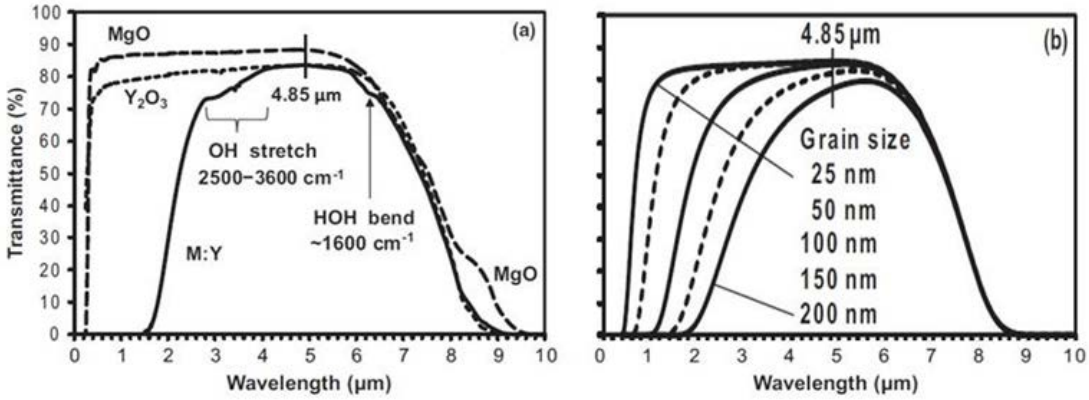

Fig. 1 a) Transmission of single crystal MgO, ceramic Y_2O_3, and 50/50 MgO:Y_2O_3 (M:Y) nanocomposite with average grain size of ~150 nm. b) Predicted transmission of 50/50 MgO:Y_2O_3 as a function of grain size.[7]

Careful control of the grain growth during preparation of these dual-phase nanocomposites will be essential to success. Generally speaking, for a collection of fine particles in contact with one another, their size will increase if the system is held at a sufficiently high temperature.[15,16] To obtain a fully dense material, high temperature is required to drive densification, ultimately leading to grain growth. If the grains start out smaller (on the order of nanometers) there is a larger driving force for densification (reduction of surface area), which leads to a smaller overall grain size at the end of the process.

Currently, ceramic composites are made by simple mechanical mixing of the components, which introduces complexities such as impurities from milling media/mixing method; settling of granules by density during slurry drying; and re-agglomeration of particles during drying.[17] Recent work on dual-phase ceramic

nanocomposites has examined transformation processing or other wet processing techniques to avoid the difficulties that arise during mechanical mixing methods.[8,11,17–21] However, most of this work examines a 1:1 ratio of the phases while we aim to explore smaller additions of a minority phase.

3. Approach

We used a one-pot co-precipitation synthesis method to synthesize nanopowder composite material consisting of a majority MgO phase and a minority Er:Y_2O_3 phase. The relatively low maximum phonon energy of Y_2O_3 (~590 cm^{-1}[22]) makes it suitable to host the RE fluorescing ion. As long as the volume fraction of the Y_2O_3 phase (TC=8-13 W/mK[23]) is kept below 15%, the effective thermal conductivity of the composite will remain close to the higher value of MgO (45–70 W/mK[24]) according to the established Bruggeman model.[25] The co-precipitation method allows for intimate mixing of the dissolved precursors before the product crystallizes and crashes out of the solution. Careful calcination of the precipitated powder leads to nanocrystallites at moderately low temperatures (<1000 °C), which is useful for preventing large grains in the final ceramic composite.

3.1 Powder Synthesis

The co-precipitation method is used to synthesize amorphous precursor powders in an aqueous environment. Prior to the chemical precipitation, a reactant solution was prepared, consisting of yttrium nitrate (high purity 99.99%), magnesium nitrate (high purity 99.99%) and erbium nitrate (high purity 99.99%) dissolved in deionized (DI) water. The total amount of water added was proportional to the solubility limit of magnesium nitrate in water. Thermogravimetric analysis was used to determine the number of grams of cations per gram hydrated nitrate. This is imperative to achieve precise concentrations of RE cations in the final material.

In addition to the reactant solution, a basic solution was made in which the chemical reaction would take place. The basic solution consisted of 2% by weight of ammonium bicarbonate in DI water with ammonium hydroxide added until a pH of ~10 was obtained. Finally, the reactant solution was added drop-wise to the basic solution in a fume hood while maintaining the pH at ~10 using small amounts of ammonium hydroxide. Once the reactant solution was exhausted, the pH was stabilized at ~10 and the resulting suspension was allowed to age overnight under constant stirring.

The next day, the suspension was filtered from the salty solution. The resulting powder was then washed in isopropyl alcohol and then filtered; this was repeated for 3 total washings. The powder was then dried in an oven at ~65 °C.

3.2 Powder Processing and Densification

Once the powder was dry, it was gently crushed and calcined at a heating rate of 10 °C/min and held at varying temperatures (700, 1000, and 1200 °C) for 30 min. Experiments later on in the program used ball milling in isopropanol and yttria milling media in an attempt to break up agglomerates. The procedure used for these experiments is discussed later.

Two different densification methods were employed. Pressureless, air-fire sintering was first explored to isolate the ideal ratio of MgO to Er:Y_2O_3. The ratio of Er:Y_2O_3 to MgO was varied around an average of 10 weight percent (5%, 10%, and 15%). This represents a compromise between having sufficiently little Er:Y_2O_3 to inhibit its[1] grain growth and limit optical scattering, and having enough to provide adequate volume-averaged Er concentration for eventual lasing. With 2% of the Y replaced by Er, the volume-averaged Er concentration for 10% Y_2O_3 is ~5×10^{19} cm^{-3}. This average is only slightly lower than the concentrations often used in laser experiments on Er:Y_2O_3 and closely related materials, and the 2% atomic in the Er:Y_2O_3 is within the range for which the upper state lifetime is reported to remain approximately constant with little quenching.[26–28] The calcined powders were loaded into a 1-cm die and uniaxially pressed into pellets approximately 3 mm thick. The pellets were then vacuum sealed in clean bags and further compressed in a cold isostatic pressure vessel. The pellets were held at a maximum pressure of 30k psig for 30 s. The pressed pellets were removed from their bags and sintered in air at 1550 °C for 1 h, with a heating rate of 10 °C/min.

The second method of densification was hot uniaxial pressing under vacuum atmosphere. An Oxy-Gon Industries refractory metal miniature hot press equipped with a linear variable differential transformer was used to track uniaxial shrinkage during the operation. A graphite die, 1 inch in diameter, was coated with boron nitride (BN) spray and dried prior to use. The powders were gently crushed in a glass mortar in pestle to obtain a fine powder before filling the die. The dies were also set in a vacuum oven (set at 80 °C) overnight to prevent any water from adsorbing to the surface of the powders. The calcined powders were loaded in between BN spacers to prevent carbon contamination from the die at high temperature.

3.3 Physical Characterization Methods

3.3.1 X-ray Powder Diffractometer (XRD) and X-ray Fluorescence (XRF)

The pressureless sintered, air-fired pellets were measured in an X-ray powder diffractometer (Rigaku MiniFlex II) to determine semiquantitative composition (MgO to Y_2O_3 ratio). Calibration specimens were batched with known MgO/Y_2O_3 ratios and measured by XRD to generate a calibration curve.

Hot pressed pellets were measured in a different X-ray powder diffractometer (Bruker D2 Phaser) to obtain XRD patterns for Rietveld analysis to determine the quantities of MgO and Y_2O_3, as well as the crystallite size of both materials. X-ray fluorescence was also used to obtain semi-quantitative elemental data.

3.3.2 Scanning Electron Microscope (SEM)

Selected pellets were fractured and imaged in a Hitachi S4700 scanning electron microscope equipped with a YAG backscatter detector to highlight the phase contrast. ImageJ, Image Processing and Analysis in Java (NIH, Bethesda, MD), was used to estimate the amount of Y_2O_3 in the specimen image. The same pellets were also ion-milled through the cross-section in a Leica TIC 3X ion mill to generate flat, polished area for further SEM observation.

3.3.3 Density

The densities of the parts were measured in a couple of different ways. The first method was standard geometric density by measuring the volume of whole pellets and dividing by the mass of the pellet. The second method was to use the Archimedes principle by weighing the standard mass and suspended mass of the pellet. The third method was to use a helium pycnometer, which measures the volume of samples by pressure differences of helium gas then divides by the mass of the sample. All 3 techniques were key to fully understanding the density of the parts as each method has its own flaws. The density of the mixture was determined by the rule of mixtures based on the targeted composition and/or the measured composition according to XRF or XRD.

3.3.4 Transmission Electron Microscope (TEM)

A small amount of calcined or uncalcined powders was suspended in ethanol, and dripped onto lacey carbon grids and dried in air for imaging in a transmission electron microscope (TEM).

3.4 Optical Characterization of Materials

3.4.1 Fluorescence

Fluorescence spectra of the ~1.5μm $^4I_{13/2} \rightarrow {}^4I_{15/2}$ and ~980 nm $^4I_{11/2} \rightarrow {}^4I_{15/2}$ infrared transitions of Er^{3+} were obtained using a Horiba iHR320 monochromator with a 1.5-micron blazed grating and equipped with a liquid nitrogen cooled extended-range indium gallium arsenide (InGaAs) photodiode for detection. Excitation at 804.1 nm into the $^4I_{9/2}$ manifold was supplied by a Spectra Physics Tsunami Ti:sapphire laser operated in continuous wave mode.

3.4.2 Fluorescence Lifetimes

Fluorescence lifetimes of the $^4I_{13/2}$ and $^4I_{11/2}$ manifolds were acquired by exciting the sample with a modulated ~808-nm laser diode. The decay signal was detected with an uncooled InGaAs photodiode equipped with a 1500-nm long-pass filter, and was analyzed using a Tektronix TDS7104 digital oscilloscope.

3.4.3 Raman

Raman measurements were performed using a Renishaw inVia confocal Raman microscope equipped with excitation lasers at 514 nm, 633 nm, and 785 nm.

3.4.4 Percent Transmission (%T)

Percent transmission measurements were performed on suitably transparent samples using a Cary 6000i (UV-vis-nIR) spectrophotometer for measuring the 0.3- to 1.7-μm region and a Perkin Elmer Spectrum 2000 Fourier-transform infrared spectroscopy for measuring the 1.5- to 12-μm region. The results from both instruments were spliced together to complete the full transmission curve.

4. Results

Initial studies focused on optimizing the synthesis parameters for the US Army Research Laboratory (ARL)-made nanopowder and nanocomposite materials, and comparing them to similar commercially available materials. This involved systematically modifying such factors as solution pH, calcination temperature and time, sintering temperature and time, MgO to Y_2O_3 ratio, and the Er^{3+} doping concentration within the Y_2O_3. For each parameter modification, the material was characterized in terms of its physical and spectral performance.

Table 1 shows the variety of processing knobs that were turned during the program. While the Director's Research Initiative (DRI) was instrumental in beginning the investigation of these materials for the intended application as a solid state laser gain media, the optimal processing conditions are not yet finalized. In fact, the processing end of this research will continue in FY18 and FY19 in an effort to finalize the optimal parameters to produce a laser gain medium.

Table 1 Synthesis and processing parameters explored during the DRI program

Processing variable	Tested range	Optimal
Solution pH	7–10	10
Calcination temp (°C)	400–1300	700–1000
Calcination time (min)	30	30
Sintering temp (°C)	1000–1500	1200
Sintering time (min)	10–60	10
Y_2O_3/MgO ratio (%)	2.5–80	2.5–5
Applied pressure during sintering	0–50 MPa	17 MPa
Er^{3+} Concentration in Y_2O_3 (at.%)	0.8–5.0	0.8

Making powders in the laboratory enabled us to determine exactly how much RE material to include in the overall composition. It also allowed for us to work with pure materials without the need for mixing, which could introduce impurities and affect the spectroscopic results. We were able to confirm particle sizes and shapes by TEM, SEM, and Brunauer-Emmitt-Teller methods. We also showed that pressureless sintering of the parts is not sufficient for producing nanoscale materials required for the high transmission. We moved on to hot pressing of the powders and found that we can reduce the size of the Y_2O_3 particles to less than 100 nm, nearing the threshold required to reach a wide range of transmission wavelengths.

4.1 Synthesis of Composite Powder

Co-precipitation of the nanocomposite powder was a logical start so that we could vary the dopant concentration as well as work toward progressing synthesis science of nanocomposite powders. Previous work has only examined the mixing of 2 pre-made powders as opposed to the 1-pot synthesis technique we developed.[7,29]

Our first synthesis experiments used a precipitation bath (the solution in which the reaction would occur), which was stabilized at a pH of 7. We were concerned that the pH could affect the precipitation of the Er:Y_2O_3. However, we found that the resulting powder was deficient in MgO, leading to a composition that was far from the target. This is due to the solubility of MgO in water. MgO forms magnesium

hydroxide quite readily in an aqueous environment. Due to the size of the particles (<20 nm upon precipitation, before calcine), this could also mean that the crystallites themselves dissolve into the neutral solution. We also found that as the resulting precipitate is washed in DI water after the reaction, more MgO dissolves in the water also decreasing the MgO concentration. To mitigate these problems, the pH of the precipitation bath was increased to 10, which is comparable to what has been conducted in the literature.[30] Once the samples were produced, we found that the pH change did not have an effect on the Er:Y_2O_3 characteristics.

To further understand the morphology of the powders, an attempt was made to image them in the SEM; however, it was found that the particles were much too small to resolve. Transmission scanning microscopy was used instead. The powder imaged was 2.5% Er:Y_2O_3 (0.8 atom percent Er) in MgO calcined at 700, 1000, and 1200 °C for 30 min; the images are shown in Figs. 2–4. These temperatures were determined based on thermogravimetric analysis/differential scanning calorimetry data and phase identification by XRD. Figure 5 shows a combined plot of sample mass and heat flow versus temperature. The major exotherm at ~300 °C is where the adsorbed water is burned off. The material is still disordered such that an XRD pattern cannot discern the phase.

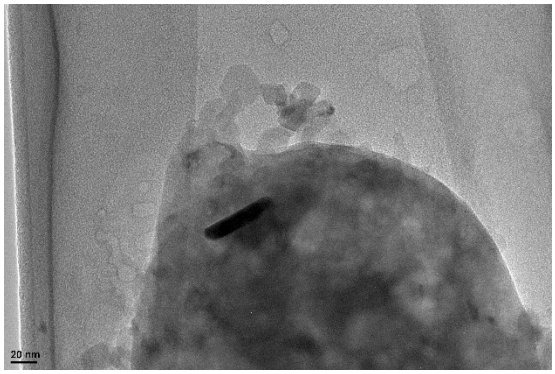

Fig. 2 Transmission electron microscope image of 2.5% Er:Y_2O_3 and MgO composite powder calcined at 700 °C in air for 30 min. This powder is not very well crystallized and has both large and small particles, which are relatively agglomerated.

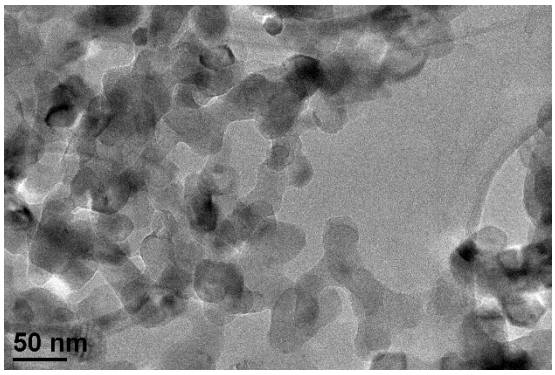

Fig. 3 Transmission electron microscope image of 2.5% $Er:Y_2O_3$ and MgO composite powder calcined at 1000 °C in air for 30 min. This material has a primary particle size of ~40 nm, which is relatively well crystallized.

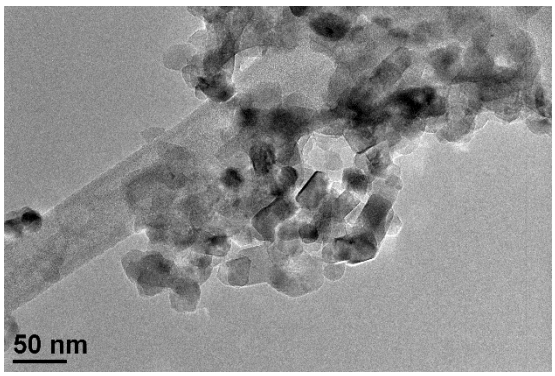

Fig. 4 Transmission electron microscope image of 2.5% $Er:Y_2O_3$ and MgO composite powder calcined at 1200 °C in air for 30 min. This material has a primary particle size of ~40 nm and is well crystallized.

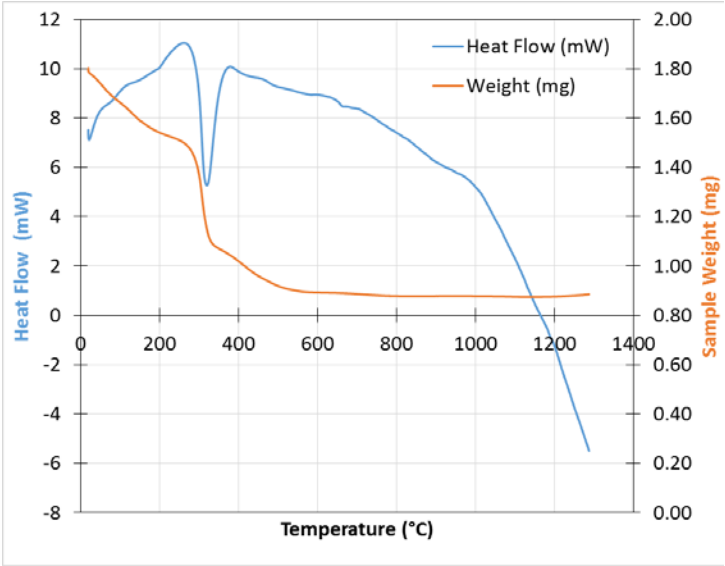

Fig. 5 Sample weight and heat flow vs. temperature of the precursor composite powder. The endotherm at ~300 °C is where major water burnout occurs.

Figure 2 shows the powder calcined at the lowest temperature. At this point in the temperature and phase development of the material, all adsorbed and chemical water is burned off and long range order is just beginning to develop. This is confirmed in the powder XRD data, shown in Fig. 6. The data has been fit to a model using the Rietveld method in Topas (Bruker Inc.) to estimate the crystallite size. The crystallite size of the MgO was calculated to be 32.5 nm. However, the Er:Y_2O_3 is not fully crystallized and is only one discernable peak in the pattern; therefore, a value cannot be calculated for the Er:Y_2O_3 using this method.

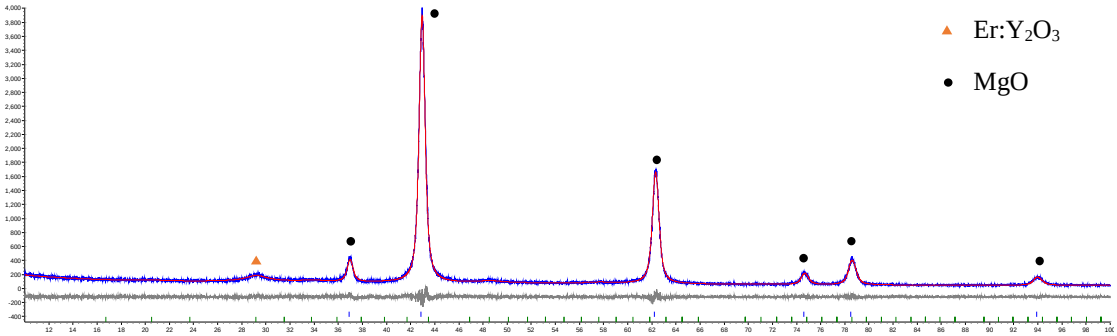

Fig. 6 Rietveld refinement of a powder diffraction pattern of 5% Er:Y_2O_3 and MgO powder calcined at 700 °C for 30 min. The orange triangle denotes a peak corresponding to Er:Y_2O_3 and the black circle corresponds to the MgO peaks.

Figure 7 shows the Rietveld fit for 5% Er:Y_2O_3 and MgO powder calcined at 1000 °C for 30 min. In this data, more Er:Y_2O_3 peaks are resolved because the Er:Y_2O_3 has begun to crystallize. The crystallite size of the MgO is calculated to be 50.4 nm, larger than the powder calcined at the lower temperature. The crystallite size of the Er:Y_2O_3 is calculated to be 156 nm. It is important to keep in mind that 5 weight percent is on the detection limit for semiquantitative XRD; therefore, the crystallite size of the Er:Y_2O_3 should be understood to be an approximation.

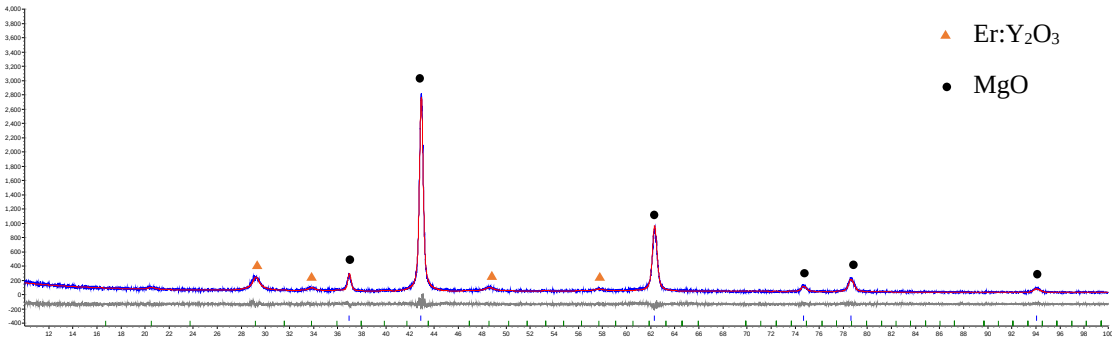

Fig. 7 Rietveld refinement of a powder diffraction pattern of 5% Er:Y_2O_3 and MgO powder calcined at 1000 °C for 30 min. The orange triangle denotes a peak corresponding to Er:Y_2O_3 and the black circle corresponds to the MgO peaks.

Overall, the XRD data and calculated crystallite sizes correlates well with the estimated primary particle sizes observed in the TEM. While a thorough size analysis of the TEM data has not yet been completed, the crystallite size calculation passes the sanity check based on the TEM images.

4.2 Pressureless Sintering of the Composite Powder

Pressureless sintering of the composite powder led to translucent materials with relatively large grains sizes. Figure 8 shows the microstructures of 2 samples, 10% Er:Y_2O_3 and 5% Er:Y_2O_3 with 10-micron scale bars. The 10% Er:Y_2O_3 sample has smaller MgO grains than the 5%. This is due to the Er:Y_2O_3 and MgO grains being pinned at the grain boundaries as both of the materials compete for grain growth. To have significant transmission in the shorter wavelengths, the grains of the Er:Y_2O_3 must be less than 100 nm. These images suggest that the Er:Y_2O_3 grain size is still too large to have significant visible light transmission.

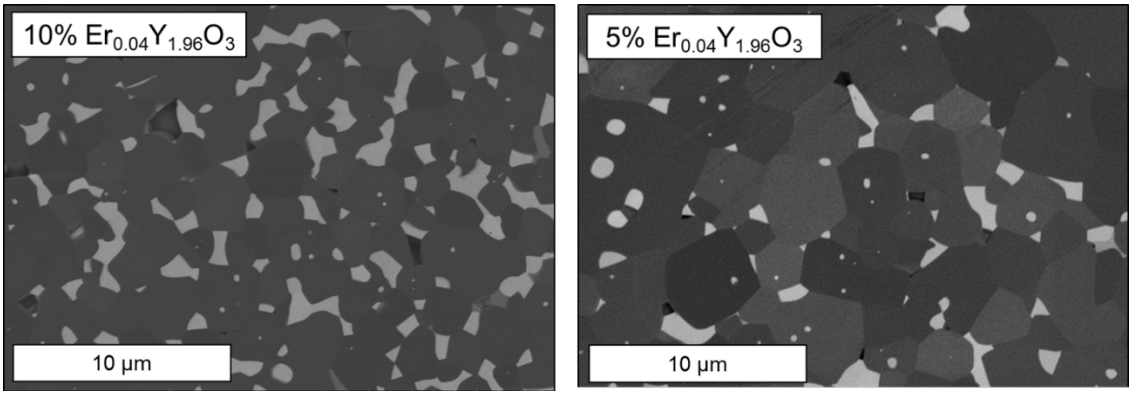

Fig. 8 Scanning electron microscopy images using a backscatter detector to enhance the different materials in the composite. The lighter phase is the Er:Y_2O_3 while the darker grains are MgO. Darker pores exist at the interstices of the grains.[29]

Figure 9 shows backlight images of the same sample pellets from Fig. 8. In this case, the samples are translucent to visible light and there are some inhomogeneities affecting light scattering. This is likely from agglomerates in the powder that were not broken up during the pressing stage of the green parts. However, the 5% sample does appear to have slightly better transmission than the 10% sample.

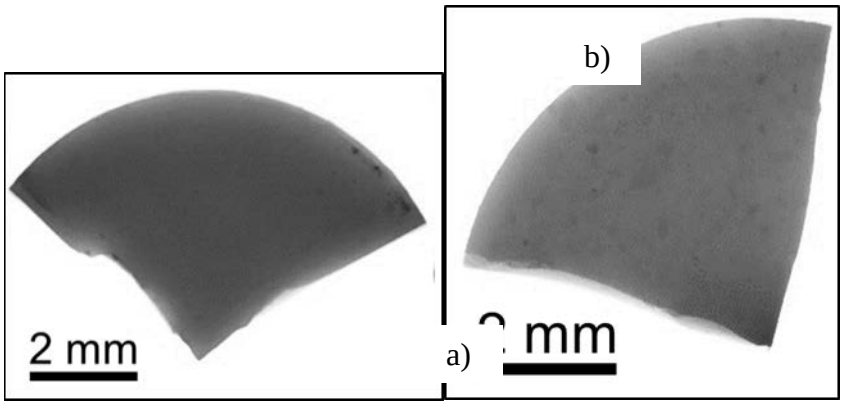

Fig. 9 Back light images of the sample pellets, a) 10% Er:Y_2O_3 in MgO and b) 5%Er:Y_2O_3 in MgO

From the pressureless sintering results, we determined that we should further decrease the amount of Er:Y_2O_3 in the composite to further isolate the Er:Y_2O_3 grains in the MgO matrix. As more Er:Y_2O_3 is added to the material, the grains will coalesce into larger grains during the densification step. If the Er:Y_2O_3 grains are small enough, the material will have improved visible light transmission.

4.3 Hot Press Sintering of Composite Powders

Hot pressing of ceramics has been widely used to produce ceramics with low porosity and small grain sizes. When pressure is added to the densification process, the maximum temperature required to get a dense sample is decreased. For example, all of these next samples were hot pressed at 1200 °C for a maximum of 30 min (under 17 MPa uniaxial pressure), while in the box furnace the samples were sintered at 1550 °C for 1 h.

The hot press also gives us the advantage of being able to track the progress of densification. Figure 10 shows an example densification curve, which was typical during the hot pressing operation of Er:Y_2O_3/MgO composite materials. As the temperature increases, the whole system (uniaxial press rams, die, sample, spacers, etc.) expands according to thermal expansion. Once densification begins, the expansion will turn into contraction. In this case, the densification began while the furnace was still increasing in temperature. Densification ceased shortly after the maximum temperature was reached. This means that the center to center of each grain was no longer moving closer to one another.

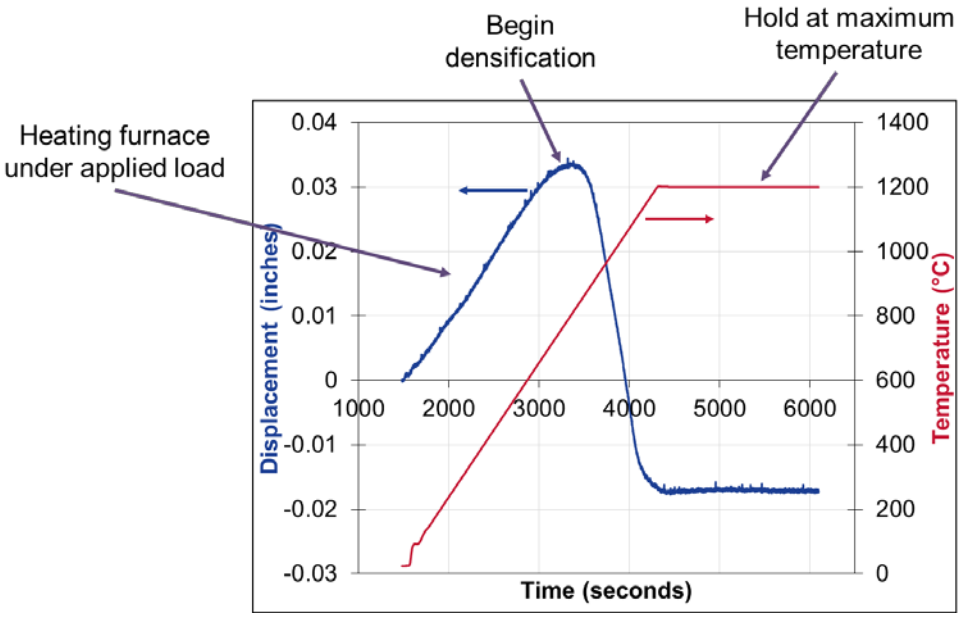

Fig. 10 Displacement and furnace temperature vs. time curves for a typical hot press experiment on Er:Y_2O_3/MgO

In all measurements, the pressure was relieved on the sample at the end of the hold so that no pressure would constrain the sample on the cool down. If pressure is on the sample during cooldown, the sample is too constrained and can crack due to thermal contraction mismatch between the 2 materials.

Data from the displacement of the rams is even more valuable when the data is corrected for the thermal expansion component during the experiment. Figure 11 shows the converted displacement data as a percent of theoretical density (TD) and temperature versus time. The bright red horizontal line indicates the maximum density of 100% of TD, which is not quite achieved in this experiment. The blue line represents the temperature of the furnace, which makes it clearer now that the material starts to densify at ~800 °C and slows down at the hold temperature of 1200 °C. This sample was held at temperature for 10 min. This plot also shows that there is some small amount of densification occurring during the hold. However, as the sample is held at the maximum temperature, the grains will continue to grow and could lead to a decrease in visible light transmission.

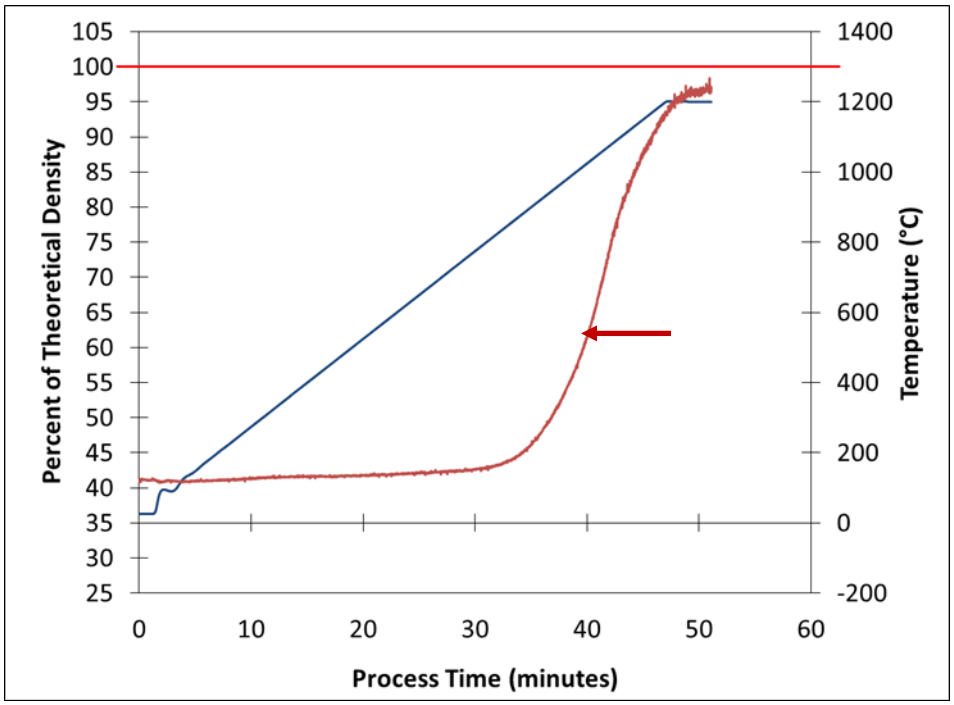

Fig. 11 The displacement curve from the hot press run of (1000/10) sample is converted to a percent of TD vs. time by hot pressing a blank die and spacers to the same experimental parameters. Then, the displacement data from the blank is subtracted from the sample experiment to remove the thermal expansion component.

Table 2 shows the processing conditions for 4 hot-pressed experiments. All 4 samples were prepared from the same original precursor powder batch. The initial batch was divided into 2 and calcined at 2 temperatures, 700 °C and 1000 °C, for 30 min each. As discussed earlier, the crystallite size of the Er:Y_2O_3 is smaller in the material calcined at 700 °C. We hypothesized that the material that was calcined at a lower temperature would have a finer grain size in the final part, which would lead to improved light transmission. Some basic data on the physical nature of the parts is also included in Table 2, including the sample thickness, density, and the percent of the TD, assumed to be 3.616 g/cm^3.[*]

[*] The theoretical density was calculated based on the targeted composition of 2.5% Er:Y_2O_3 and balance MgO by using the rule of mixtures.

Table 2 Sample calcination and hot pressing parameters and thicknesses for the transparent dual-phase nanocomposites studied

Sample No.	Powder calcine temp/time	Hot-press temp/dwell time	Sample thickness (cm)	Sample density (g/cm^3)	Percent of TD (%)
1	1000 °C/30 min	1200 °C/30 min	0.114	3.597	99.5
2	700 °C/30 min	1200 °C/30 min	0.118	3.601	99.6
3	700 °C/30 min	1200 °C/10 min	0.171	3.562	98.5
4	1000 °C/30 min	1200 °C/10 min	0.117	3.613	99.9

All samples except for Sample 3 had a density greater than or equal to 99.5% of the TD. Sample 3 had the lowest calcination temperature and the shortest hold time in the hot press, leading to the least amount of heat work applied to the material; less work on the sample could lead to lower sintering rates and more porosity. Figure 12 shows a backscatter SEM image of Sample 3; the light phase is the Er:Y_2O_3 and the grey phase is the MgO. Pores are scattered around the surface and are approximately the same size as the Er:Y_2O_3. In this case, more time, higher temperature, or greater pressure could improve the density and, hence, the transmission.

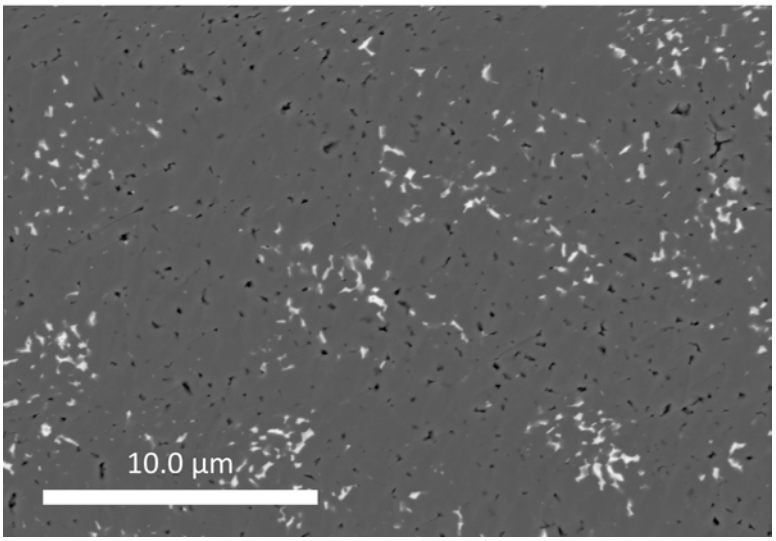

Fig. 12 Backscatter SEM image of sample 3 with a 10 micron scale bar

Figure 13 shows Sample 1 a) on the left and Sample 4 b) on the right, both with 20-micron scale bars. The immediate observation is that Sample 4 has a smaller overall grain size than Sample 1. Both samples were from powder that was calcined at 1000 °C for 30 min, the only difference being that the hold temperature was

shorter (10 min) for Sample 4. This indicates that once the densification process is complete, the only real changes that occur to the microstructure is grain growth.

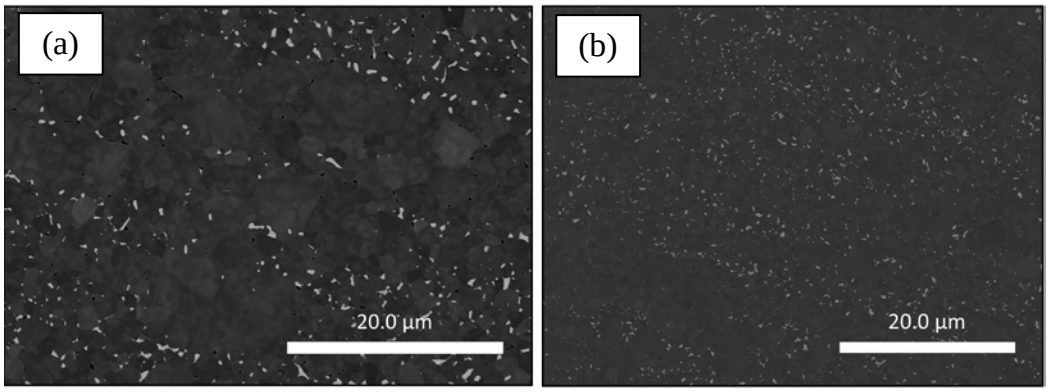

Fig. 13 Backscatter SEM images of a) sample 1 and b) sample 2

The other main observation in the microstructure is the bands of Er:Y_2O_3. This is likely due to aggregation of the particles during the calcination process—these aggregates are not broken up during the gentle crushing before hot pressing, leading to an inhomogeneous microstructure. The banding effect is due to the uniaxial pressure on the samples during densification, the bands are perpendicular to the pressing direction. Another interesting effect is that the MgO grains are much larger in areas where there are limited Er:Y2O3 grains. In these areas, there is not enough Y_2O_3 to limit the grain growth of the MgO by grain boundary pinning. These areas with large grains also have pores that remain at the triple points. The main way to alleviate these microstructural inhomogeneities is to break up the aggregates prior to hot pressing by some sort of milling step.

4.4 Spectral Characterization of Parts

Spectroscopic characterization was employed to gauge the quality of our nanocomposite materials as compared to the current state-of-the-art ceramics from Konoshima Corp (Japan). Figure 14a shows a comparison between the Konoshima Er:Y_2O_3 ceramic and ARL-produced materials. The fact that our materials look identical to the benchmark ceramic indicates that the local environment of the Er is similar. This is encouraging to see, especially in the nanocomposite material, because it means that the RE is preferentially doped into the Y_2O_3 as intended and not in the MgO. Figure 14b shows fluorescence lifetime trends for the $^4I_{13/2}$ level of Er for a series of Y_2O_3 nanopowder samples with varying Er concentrations and with different calcination temperatures. Comparing these values to those in Figure 14c, which depicts the lifetime trends in the Konoshima ceramic benchmark material, we see that the only ARL sample that closely matches is the 0.8 at.% Er:Y_2O_3 calcined at 1200 °C. In fact, the trends with Er concentration between the

2 sample groups are anti-correlated, where the Konoshima samples demonstrate increasing lifetime with Er concentration, ARL made materials show decreasing lifetimes with increasing amounts of Er. The increasing lifetime trend for the Konoshima samples is understood to be a result of a growing reabsorption effect for the higher Er concentrations, whereas the decreasing trend in the ARL samples is indicative of a lifetime quenching phenomenon (such as upconversion) that increases when more Er is added to the material. Indeed, the quenching effect is strong enough to counteract the lifetime lengthening that should arise from reabsorption, and might be indicative of severe clustering in our samples. More information can be gleaned from the fact that the lifetimes decrease with decreasing calcination temperature. These shorter lifetimes than the Konoshima benchmark materials also imply a degree of quenching in the low-T prepared samples; however, this time the lifetime shortening is attributed to lower crystalline quality of the Y_2O_3. This conclusion is supported by the degraded fluorescence spectra that were observed from these samples. The spectroscopic measurements of this series of ARL samples were instrumental in planning future synthesis runs, as they guided us to focus more on low Er concentrations and higher calcination temperatures.

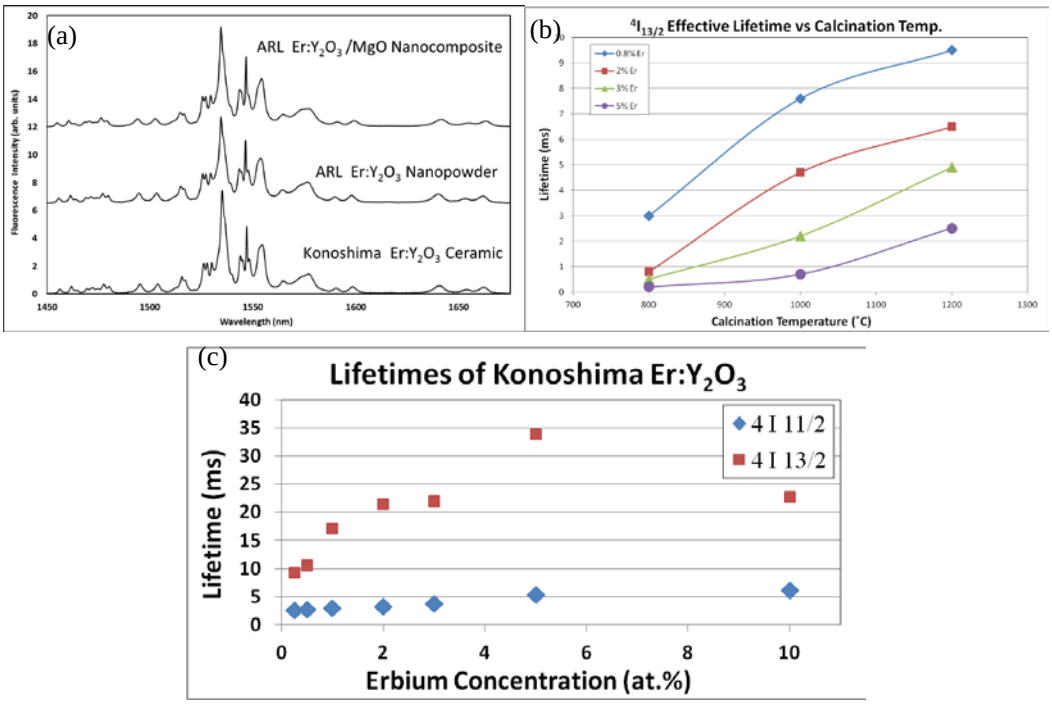

Fig. 14 a) Comparison between Konoshima commercial $Er:Y_2O_3$ ARL-produced nanopowders and nanocomposites. b) Effective lifetimes of the $^4I_{13/2}$ Er level for doped Y_2O_3 nanopowders under different growth conditions. c) Fluorescence lifetimes vs. erbium concentration in Konoshima ceramics.

Measurements of the Raman spectrum of the ARL-made nanocomposites were performed to determine the effect that the dual-phase system would have on the low-maximum-phonon Y_2O_3 component. Of the 3 available excitation wavelengths on the Renishaw Raman microscope, the 785-nm line was found to be best due to the fact that it has the least overlap with the absorption from the incorporated Erbium dopant in our samples. Even for this excitation, however, Fig. 15a shows that the spectra obtained from the Raman instrument are very complicated. By comparison with the known energy levels of RE materials in Y_2O_3, we were able to identify the majority of the peaks as various fluorescence transitions. As seen in Fig. 15a, the peaks in the short-wavelength region are from the $^4I_{9/2} \rightarrow {}^4I_{15/2}$ transition in Er, while the peaks in the long-wavelength region are from the $^4F_{3/2} \rightarrow {}^4I_{9/2}$ transition in neodymium (Nd). The set of peaks in the middle of the spectrum originate from the up-converted $^4S_{3/2} \rightarrow {}^4I_{13/2}$ transition in Er. There is only one actual Y_2O_3 Raman peak observed at ~379 cm^{-1}, as shown in Fig. 15a.

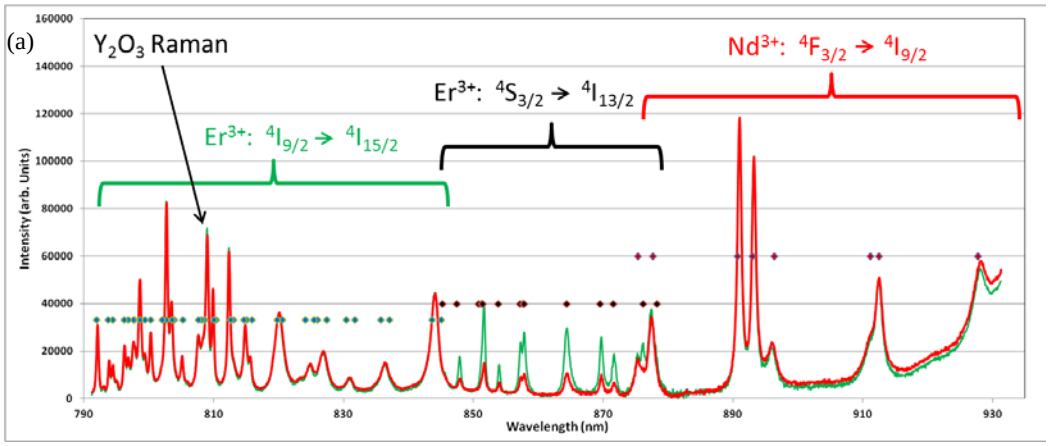

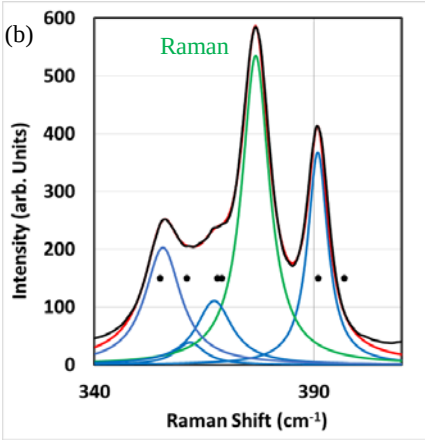

(c)

Material Type	Average Raman Center (cm^{-1})	FWHM (cm^{-1})
Konoshima ceramics ($Er:Y_2O_3$)	379.3	7-8
WMRD Powders ($Er:Y_2O_3$)	379.8	7-9
WMRD Powders ($Er:Y_2O_3$/MgO)	380.7	8-10
WMRD Densified ($Er:Y_2O_3$/MgO)	382.5	8
WMRD Densified ($Er:Y_2O_3$)	378.9	6.8

Fig. 15 a) Spectra obtained from Er:Y_2O_3/MgO nanocomposites using the Renishaw Raman microscope including both Raman and RE fluorescence peaks. b) Spectrum in the immediate vicinity of the Y_2O_3 Raman peak, including curve fittings and expected Erbium energy levels (dots). c) Trends for the average center position and FWHM of the Y_2O_3 Raman peak for various sample types.

Even before studying this 1 Raman peak, a number of observations can be made based on the "unwanted" fluorescence. The fact that all 3 spectral transitions present in the graph are of similar intensity to the Raman peak (which is known to be a very weak phenomenon) means that these peaks are similarly weak. It is simply because of the high sensitivity of the Raman instrument that these peaks show up at all. We tried to measure this spectrum with our regular fluorescence setup using the same excitation wavelength, but the fluorescence peaks were too weak to observe. The fact that Nd peaks were observed, after only actively doping Er into the material, was unexpected but not unheard of: there are often trace amounts of other RE species present even in high purity precursors. A piece of this sample was sent out to Galbraith Inc. for elemental analysis, and the results showed Nd concentration was less than 30 ppm.

Aside from demonstrating the presence of Nd, the "unwanted" fluorescence actually proved beneficial in the characterization of our samples. Figure 15a actually shows 2 spectral curves: a green one representing material that was synthesized in a solution of pH 7 and a red one synthesized at pH 10. Every other preparation parameter (species ratios, Er concentration, calcination times, etc.) was held constant between the 2 materials. When comparing relative peak heights between the samples, for most of the graph there is good overlap between the 2 spectra. However, for the middle set of peaks, representing the up-converted Er fluorescence, there is divergent behavior: the pH 7 sample shows increased relative fluorescence intensity than the pH 10 sample. This is significant because, unlike the other transitions, the middle peaks originate from an up-conversion (and, therefore, nonlinear) process and are likely indicative of Er clustering.

Due to the complicated nature of the spectrum shown in Fig. 15a, curve-fitting had to be employed to isolate the Raman peak from the surrounding fluorescence to allow for characterization. Figure 15b shows the immediate spectral region of the Y_2O_3 Raman peak and includes deconvoluted Lorentzian fits for all peaks in the area. The dots represent where we would expect to find Er transitions based on the energy levels in this host material. Through this method of isolating the Raman peak, we could record important characteristics such as the average Raman shift and the full width-half maximum (FWHM). Figure 15c shows the results of analysis of several different sample types including the Konoshima benchmark materials and ARL-made materials. It was observed that the presence of nearby MgO in the nanopowders and nanocomposites has the slight effect of shifting the average Raman center by ~3 cm^{-1}, which is small enough of a change to negligibly affect the performance of the laser gain material operating in the mid-IR spectral region. Additionally, there is no significant difference in the Raman FWHM between

Konoshima ceramics and ARL-made nanocomposites, indicating a comparable crystal quality.

When samples of sufficient transparency were prepared, percent transmission (%T) measurements were performed. The specific details for the transparent samples studied were shown in Table 2. The variations in calcination temperature–time and sintering temperature–time were implemented to determine how these parameters affect grain size and, thus, transmissivity. Conventional wisdom dictates that higher processing temperatures should lead to larger grain growth. Some conditions were held constant across all the samples in this study. For instance, all samples were composed of 2.5 wt% Y_2O_3, and that component was doped with 0.8 at.% Er. (However, the Er content is inconsequential for this particular measurement.) The density of all the produced parts were measured using the Archimedes principle, and the percent of TD was calculated based on a TD of the mixture being 3.616 g/cm^3.

Percent transmission spectra were obtained for each of these samples, and the transmission data was compared to theoretical curves generated by a Mie scattering model to determine the average grain size of the Y_2O_3 minority component in the dual-phase nanocomposites. In the course of fitting the experimental transmission curves, the standard operating procedure was to attach priority to fitting the scattering band edge on the short-wavelength side of the curve and also trying to conform to the high points of the curve as much as possible. The absorption edge on the long wavelength side of the graph was considered less important because it did not directly impact the *a* parameter determination. Unfortunately, in most cases, there could be found no *a* value that fit well in both high-priority regions. There seemed to be a tradeoff between having a too-low fit on the left with a decent fit on the top, and having a decent fit on the left with a too-high fit on the top. In an effort to achieve fits in both regions, the authors tried a new tactic of implementing a <1 wavelength-independent scale factor *z* to the calculated fits. With adjustment of both *a* and *z*, decent fits were found for all samples. Such a broadband reduction in the calculated transmission curve is not unwarranted because the sample surfaces were not polished, which would lead to overall higher surface scattering losses. Figure 16 shows the recorded percent transmission spectra for the MgO/Er:Y_2O_3 nanocomposite samples measured in this study, as well as the *z*-modified fit curve for each. In addition, there is an "unmodified" fit that represents the same scattering calculation without employing the *z* factor.

The experimental curves in Fig. 16 show much more structure than is present in the fittings. The 2 main classes of structures observed are the relatively sharp absorption features toward the center of the graph and the rather sharp drop in transmission between 6 and 7 μm, which deviates significantly from theoretical

predictions. The former is probably related to some amount of unknown impurities in the sample. The latter may well originate from unwanted contamination from BN, which was used to coat the die spacers during sintering. Published infrared absorption spectra of BN show a strong absorption peak starting right around 6–7 microns.[31]

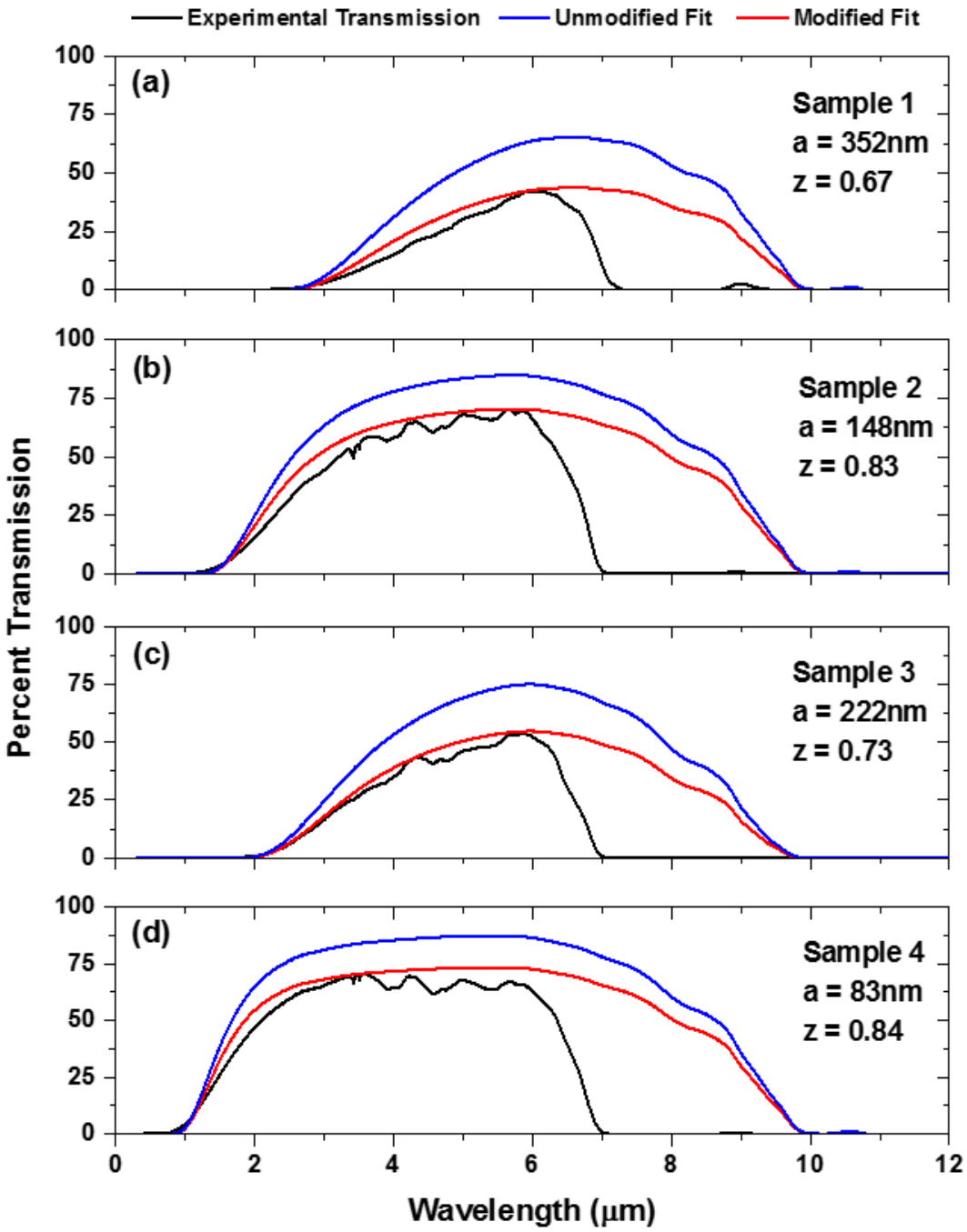

Fig. 16 Experimental percent transmission (black curve) and 2 fit curves (best fit [red] and maximum transmission possible [blue]) for the MgO/Y_2O_3 nanocomposite samples measured; also scattering particle diameter a and modification factor z for each

Figure 16 includes the *a* values used in calculating the curve fits for each sample. These range from 83 nm for Sample 4 to 352 nm for Sample 1. The clearest trend can be seen in these 2 bookend samples, both of which were calcined at 1000 °C for 30 min and both of which were hot-pressed at 1200 °C. The difference between them, as shown in Table 2, is that Sample 1 was hot pressed for 30 min while Sample 4 dwelled at its maximum temperature for only 10 min. The extra time that Sample 1 was subjected to the high temperature treatment represents a much greater propensity for grain growth, and this was exhibited in the greater degree of scattering in this sample. These results correlate well with the relatively larger Y_2O_3 grain observed in the SEM image of Sample 1 shown in Figure 13a.

The fit curves for Samples 2 and 3 dictate *a* values in the middle of the range; however, these results did not follow as clear a trend. These samples contain material calcined at 700 °C for 30 min, with the same variation in hot-pressing times experienced by the previously discussed samples. One would expect that Sample 2, with its longer hot-pressing dwell time, would exhibit more scattering than Sample 3. Yet, the observations are just the opposite. Recall that the lower calcination temperature employed in the processing of these samples was chosen to reduce particle agglomeration. One possibility for this unexpected result is that the relatively low calcine temperatures resulted in material that was not fully nucleated, and that Sample 2, with its longer hot-press dwell time, was able to overcome this issue better than Sample 3 with its shorter hot-press dwell time. Such a phenomenon was observed in previous sample batches prepared at similar temperatures.

One final consideration that could explain the discrepancies between theoretical and experimental transmission is the porosity of the nanocomposites. The density of parts (listed in Table 2) is indicative of the remnant porosity in the samples. Any remnant porosity in these parts will influence the raw transmittance of the part as the pores will have a refractive index of the atmosphere inside the pore. Since these were processed under a vacuum (on the order of 10-5 torr), it is reasonable to assume that the trapped pores are under vacuum. However, there is still the possibility of pores affecting the overall scattering in the samples. Future improvements to Mie scattering calculations will attempt to account for the scattering caused by the porosity.

5. Conclusions

Over the course of this 3-year DRI project, considerable progress was made toward a functional laser gain material based on a dual-phase nanocomposite material. A novel, 1-pot synthesis technique was employed to produce nanocomposite powders with limited impurities and fine crystallite size upon calcination. These

nanopowders served as the precursor to densified nanocomposite parts. ARL-made Er:Y_2O_3/MgO nanopowders and nanocomposites were compared to state-of-the-art Er:Y_2O_3 ceramic benchmark samples obtained from Konoshima Inc (Japan) to compare their spectral and physical qualities. Feedback from physical and optical characterizations led toward optimization of the synthesis conditions such that translucent nanocomposites were eventually realized. The work started in this DRI project to improve the light transmission of these nanocomposite materials will continue under a materials and manufacturing science division-funded program (Materials and Manufacturing Science Division RDRL-WMM).

6. References

1. Taczak TM, Killinger DK. Development of a tunable, narrow-linewidth, cw 2.066-μm Ho:YLF laser for remote sensing of atmospheric CO2 and H2O. Appl Opt 1998;37:8460–8476.

2. Clarkson WA. Thermal effects and their mitigation in end-pumped solid-state lasers. Journal of Physics D: Applied Physics. 2001;34:2381.

3. Koechner W. Solid-state laser engineering. 6th ed. Optical Sciences. New York (NY): Springer; 2006. Vol. 1. p. 748.

4. Dong J, Shirakawa A, Ueda K.-i, Yagi H, Yanagitani T, Kaminskii AA. Laser-diode pumped heavy-doped Yb:YAG ceramic lasers. Opt Lett. 2007;32:1890–1892.

5. Qi Y, Zhu X, Lou Q, Ji J, Dong J, Wei Y. Nd:YAG ceramic laser obtained high slope-efficiency of 62% in high power applications. Opt Express. 2005;13:8725–8729.

6. Kong J, Tang DY, Chan CC, Lu J, Ueda K, Yagi H, Yanagitani T. High-efficiency 1040 and 1078 nm laser emission of a Yb:Y2O3 ceramic laser with 976 nm diode pumping. Opt Lett. 2007;32:247–249.

7. Harris DC, Cambrea LR, Johnson LF, Seaver RT, Baronowski M, Gentilman R, Nordahl SC, Gattuso T, Silberstein S, Rogan P, et al. Properties of an infrared-transparent MgO:Y2O3 nanocomposite. Journal of the American Ceramic Society. 2013;96:3828–3835.

8. Jiang D, Mukherjee AK. Spark plasma sintering of an infrared-transparent Y2O3–MgO nanocomposite. Journal of the American Ceramic Society. 2010;93:769–773.

9. Muoto CK, Jordan EH, Gell M, Aindow M. Phase Homogeneity in Y2O3–MgO nanocomposites synthesized by thermal decomposition of nitrate precursors with ammonium acetate additions. Journal of the American Ceramic Society. 2011;94:4207–4217.

10. Muoto CK, Jordan EH, Gell M, Aindow M. Effects of precursor chemistry on the structural characteristics of Y2O3–MgO nanocomposites synthesized by a combined Sol–Gel/thermal decomposition route. Journal of the American Ceramic Society. 2011;04:372–381.

11. Wang J, Chen D, Jordan EH, Gell M. Infrared-transparent Y2O3–MgO nanocomposites using Sol–Gel combustion synthesized powder. Journal of the American Ceramic Society. 2010;93:3535–3538.

12. Xu S, Li J, Li C, Pan Y, Guo J. Hot pressing of infrared-transparent Y2O3–MgO nanocomposites using Sol–Gel combustion synthesized powders. Journal of the American Ceramic Society. 2015;98:1019–1026.

13. Xu S, Li J, Li C, Pan Y, Guo J. Infrared-transparent Y2O3–MgO nanocomposites fabricated by the glucose Sol–Gel combustion and hot-pressing technique. Journal of the American Ceramic Society. 2015;98:2796–2802.

14. Apetz R, van Bruggen MPB. Transparent alumina: a light-scattering model. Journal of the American Ceramic Society. 2003;86:480–486.

15. Kingery WD, Bowen HK, Uhlmann DR. Introduction to ceramics. 2nd ed. New York, (NY): John Wiley & Sons; 1976. p. 1032.

16. Rahaman MN. Ceramic processing and sintering. 2nd ed. Boca Raton (FL): CRC Press; 2003.

17. Stefanik T, Gentilman R, Hogan P. Nanocomposite optical ceramics for infrared windows and domes. Proc. SPIE 6545, Window and Dome Technologies and Materials X, 65450A; 2007 May 2; doi:10.1117/12.719312.

18. Beecroft LL, Ober C K. Nanocomposite materials for optical applications. Chemistry of Materials. 1997;9:1302–1317.

19. Kear BH, Colaizzi J, Mayo WE, Liao SC. On the processing of nanocrystalline and nanocomposite ceramics. Scripta Materialia. 2001;44:2065–2068.

20. Chawla S, Jayanthi K, Chander H, Haranath D, Halder SK, Kar M. Synthesis and optical properties of ZnO/MgO nanocomposite. Journal of Alloys and Compounds. 2008;459:457–460.

21. Llusar M, Royo V, Badenes JA, Tena MA, Monrós G. Nanocomposite Fe2O3–SiO2 inclusion pigments from post-functionalized mesoporous silicas. Journal of the European Ceramic Society. 2009;29:3319–3332.

22. Repelin Y, Proust C, Husson E, Beny JM. Vibrational spectroscopy of the C-form of yttrium sesquioxide. Journal of Solid State Chemistry. 1995;118:163–169.

23. Snetkov IL, Silin DE, Palashov OV, Khazanov EA, Yagi H, Yanagitani T, Yoneda H, Shirakawa A, Ueda K-i, Kaminskii AA. Study of the thermo-optical constants of Yb doped Y2O3, Lu2O3 and Sc2O3 ceramic materials. Opt Express. 2013;21:21254–21263.

24. Slack GA. Thermal conductivity of MgO, Al_2O_3, $MgAl_2O_4$, and Fe_3O_4 crystals from 3 to 300K. Physical Review. 1962;126:427–441.

25. Angle JP, Wang Z, Dames C, Mecartney ML. Comparison of two-phase thermal conductivity models with experiments on dilute ceramic composites. Journal of the American Ceramic Society. 2013;96:2935–2942.

26. Ter-Gabrielyan N, Merkle LD, Newburgh GA, Dubinskii M, Resonantly-pumped Er3+:Y2O3 ceramic laser for remote CO2 monitoring. Laser Physics. 2009;19:867–869.

27. Ter-Gabrielyan N, Merkle LD, Ikesue A, Dubinskii M. Ultralow quantum-defect eye-safe Er:Sc2O3 laser. Opt Lett. 2008;33:1524–1526.

28. Li T, Beil K, Kränkel C, Huber G. Efficient high-power continuous wave Er:Lu_2O_3 laser at 2.85 μm. Opt Lett. 2012;37:2568–2570.

29. Blair VL, Fleischman ZD, Merkle LD, Ku N, Moorehead CA. Co-precipitation of rare-earth-doped Y2O3 and MgO nanocomposites for mid-infrared solid-state lasers. Appl Opt. 2017;56:B154–B158.

30. Vatsha B, Tetyana P, Shumbula PM, Ngila JC, Sikhwivhilu LM, Moutloali RM. Effects of precipitation temperature on nanoparticle surface area and antibacterial behaviour of Mg(OH)2 and MgO nanoparticles. Journal of Biomaterials and Nanobiotechnology. 2013;4:365–373.

31. Chore SM, Chaudhari GN, Manorama SV, Bath A. Structural and electrical properties of cubic boron nitride thin films on (100)GaAs. Semicond Sci Tech. 2002;17:1141–1143.

Documented course of this research

Papers and Technical Reports

Fleischman Z, Blair V, Merkle L, Ku N. Size Determination of Y2O3 Crystallites in MgO Composite Using Mie Scattering. Aberdeen Proving Ground, (MD): Army Research Laboratory: (US); 2017 Nov. Report No.: ARL-TR-8206.

Ku N, Blair VL, Behler KD. Processing and characterization of zinc sulfide and calcium fluoride composite ceramics. PacRim12 Conference Proceedings, 2017 May. Second composite system explored under the realm of the DRI.

Blair V, Fleischman ZD, Merkle LD, Ku N, Moorehead CA. Co-precipitation of RE-Doped Y2O3 and MgO nanocomposites for mid-infrared solid-state lasers. Applied Optics.2017;56(3).

Conference Presentations

Fleischman Z, Blair V, Merkle L, Ku N. Dual-phase Er:Y2O3/MgO nanocomposites for mid-infrared solid state lasers. Accepted for Oral Presentation at SPIE DSS 2018.

Blair V, Fry A, Kilczewski S, Fleischman Z. Densification and sintering of ceramic nanocomposites for mid-IR solid state lasers. 7th International Congress on Ceramics; 2018 June; Foz do Iguacu, Brazil. Abstract Submitted for Oral Presentation.

Invited Keynote Presentation at the 12th International Conference on Ceramic Materials and Components for Energy and Environmental Applications (CMCEE-12); July 201; Singapore. Abstract shall be submitted upon approval.

Blair V, Ku N, Fleischman Z. Balancing microstructure and spectroscopic behavior of nanocomposites for mid-infrared solid-state lasers. ICACC 2018. Invited Oral Presentation.

Blair V, Fleischman Z, Ku N. High temperature processing of advanced nanocomposite ceramics for IR solid state lasers. MS&T 2017. Invited Oral Presentation.

Blair V, Ku N, Fleischman Z, Merkle L. Densification and translucency in RE:Y2O3 + MgO nanocomposites for mid-infrared solid-state lasers. ICACC 2017. Oral Presentation.

Blair V, Fleischman Z, Ku N, Merkle L. Er:Y_2O_3+MgO nanocomposites for mid-IR solid-state lasers. MS&T 2016. Oral Presentation.

Briefings

Blair V. High temperature processing of advanced nanocomposite ceramics for IR solid state lasers. Directed Energy Working Group Meeting, 2017 Nov 14.

Blair V. Synthesis and processing of transparent ceramic nanocomposites. Open Campus Open House, Poster and Laboratory Tour, 2017 Oct.

This work has been published in Applied Optics: Blair V, Fleischman ZD, Merkle LD, Ku N, Moorehead CA. Co-precipitation of RE-doped Y_2O_3 and MgO nanocomposites for mid-infrared solid-state lasers. Applied Optics. 2017;56(3).

List of Symbols, Abbreviations, and Acronyms

ARL	US Army Research Laboratory
BN	boron nitride
DI	deionized
DRI	Director's Research Initiative
Er	erbium
Er:Y_2O_3	erbium:yttrium oxide
FWHM	full width-half maximum
InGaAs	indium gallium arsenide
IR	infrared
MgO	magnesium oxide
Nd	neodymium
RE	rare earth
SEM	scanning electron microscope
TD	theoretical density
TEM	transmission electron microscope
XRD	x-ray diffraction
XRF	x-ray fluorescence
YAG	yttrium aluminum garnet
Y_2O_3	yttrium(III) oxide

1 (PDF) DEFENSE TECHNICAL INFORMATION CTR DTIC OCA

2 (PDF) DIR ARL
IMAL HRA
RECORDS MGMT
RDRL DCL
TECH LIB

1 (PDF) ARL
RDRL SEE L
Z FLEISCHMAN